Label-free proteomic comparison reveals ciliary and nonciliary phenotypes of IFT-A mutants

Janelle C. Leggere[a], Jaime V.K. Hibbard[a], Ophelia Papoulas[a], Chanjae Lee[a], Chad G. Pearson[b], Edward M. Marcotte[a], and John B. Wallingford[a,*]
[a]Department of Molecular Biosciences, University of Texas at Austin, TX 78712; [b]Anschutz Medical Campus, Department of Cell and Developmental Biology, University of Colorado, Aurora, CO 80045

ABSTRACT DIFFRAC is a powerful method for systematically comparing proteome content and organization between samples in a high-throughput manner. By subjecting control and experimental protein extracts to native chromatography and quantifying the contents of each fraction using mass spectrometry, it enables the quantitative detection of alterations to protein complexes and abundances. Here, we applied DIFFRAC to investigate the consequences of genetic loss of Ift122, a subunit of the intraflagellar transport-A (IFT-A) protein complex that plays a vital role in the formation and function of cilia and flagella, on the proteome of *Tetrahymena thermophila*. A single DIFFRAC experiment was sufficient to detect changes in protein behavior that mirrored known effects of IFT-A loss and revealed new biology. We uncovered several novel IFT-A–regulated proteins, which we validated through live imaging in *Xenopus* multiciliated cells, shedding new light on both the ciliary and non-ciliary functions of IFT-A. Our findings underscore the robustness of DIFFRAC for revealing proteomic changes in response to genetic or biochemical perturbation.

SIGNIFICANCE STATEMENT

- Cilia are essential organelles that govern development and homeostasis across the tree of life, but how the many hundreds of ciliary proteins act in concert remains poorly understood.

- Using an unbiased approach called DIFFRAC, we compare the proteome of normal *Tetrahymena* with that of mutants in the intraflagellar transport system; we identified a large number of protein alterations and confirmed several with experiments in Xenopus.

- Our results demonstrate the efficacy of DIFFRAC for proteome comparisons and provide new insights into ciliogenesis.

INTRODUCTION

Proper regulation of proteome content and organization is crucial for virtually all cellular functions. Therefore, understanding the impact of biochemical or genetic perturbation on the proteome is an important challenge (Gingras *et al.*, 2019; Monti *et al.*, 2019; Bludau, 2021; Low *et al.*, 2021). We recently developed differential fractionation (DIFFRAC), a method for high-throughput, systematic comparison of proteome content and organization between samples (Mallam *et al.*, 2019; Drew *et al.*, 2020; Floyd *et al.*, 2021). In DIFFRAC, control and experimental protein extracts are independently subjected to size-exclusion chromatography (SEC) and the contents of each fraction are independently quantified by mass spectrometry. Alterations in elution profiles or abundance reveal
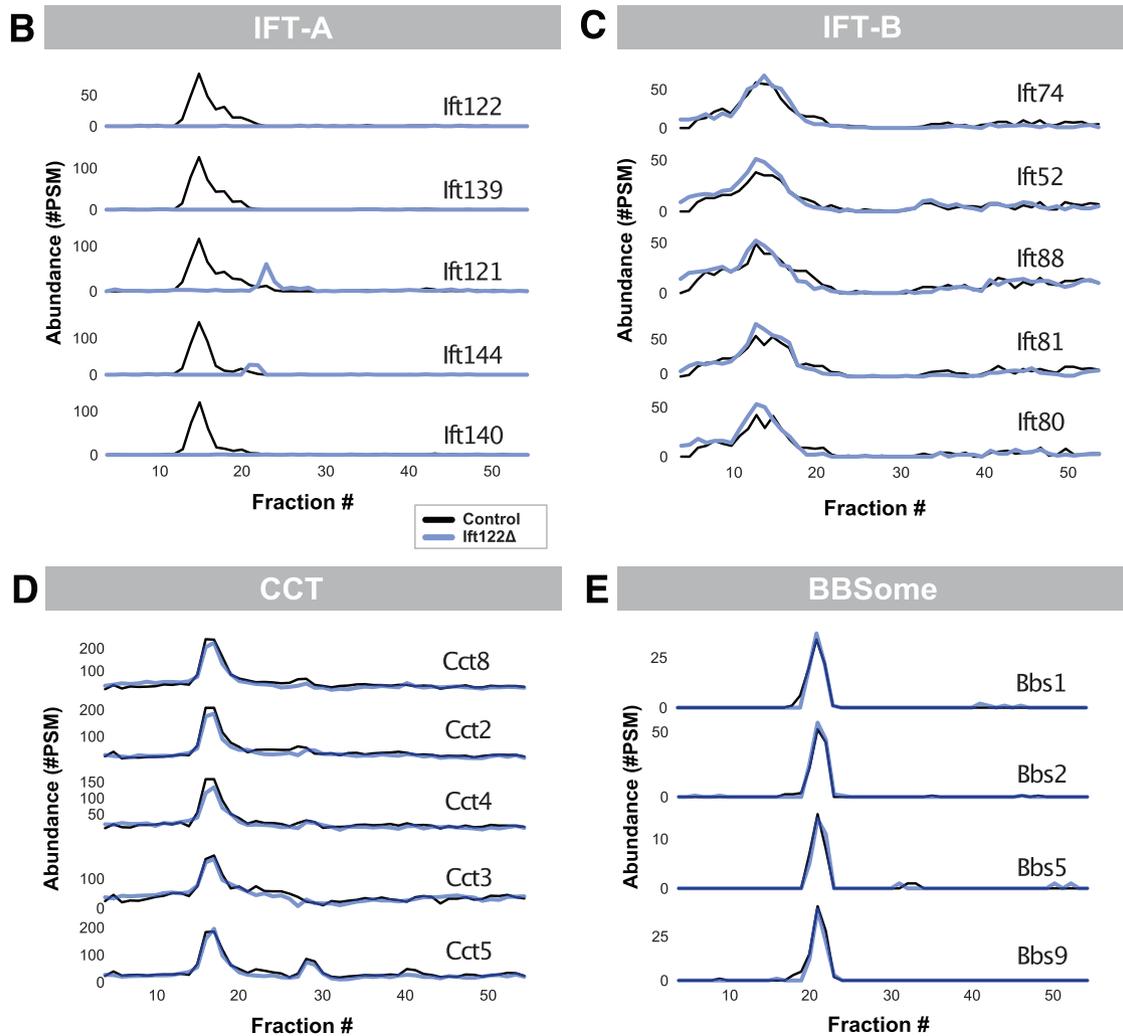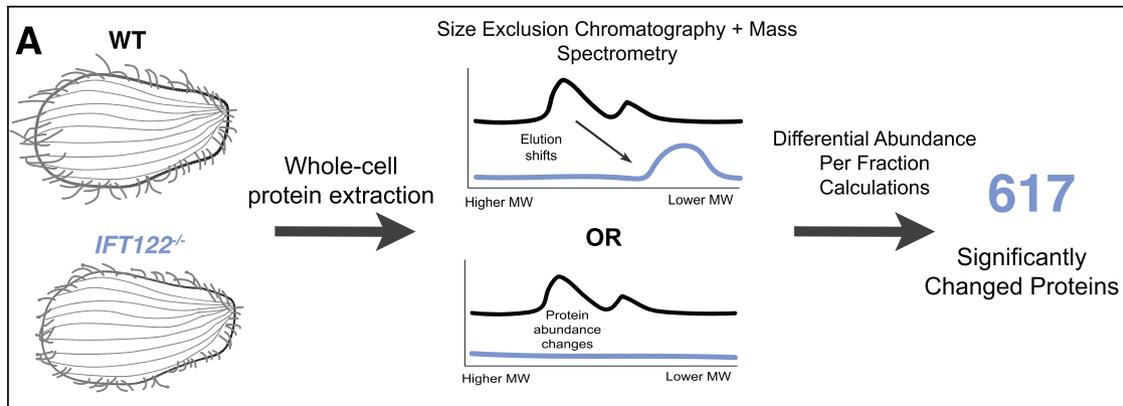
FIGURE 1: Ift122 *Tetrahymena* DIFFRAC detects specific and predicted changes in protein abundance and organization. (A) Experimental and computational pipeline overview. Samples of whole-cell wild-type or *Ift122*-null strains were lysed under nondenaturing conditions. Size-exclusion HPLC and subsequent mass spectrometry were used to determine the identity and abundance of proteins in fractions with high protein content. Differential abundance between the wild-type and null samples was calculated for every protein observed, for every fraction in which it was observed in either sample. *P*-values and FDRs were calculated for the largest (positive or negative) z-score for each protein, and 617 orthogroups which rose above the FDR cutoff of 0.1% were further analyzed. (B–E) Elution profiles show nonciliary and select ciliary protein complexes are intact in the Ift122 mutant, but IFT-A abundance and assembly are drastically perturbed. Profiles display elution behavior of select orthogroup in wild-type (black) and *Ift122*-null (blue) samples. Each row plots abundance of an individual orthogroup across all fractions analyzed. Members of known protein complexes are grouped together. (B) The abundance of each observed IFT-A subunit is drastically decreased. Additionally, the later elution of IFT144 and IFT121 in the mutant suggests the remaining subunits are present in a smaller, lower molecular weight complex in the *Ift122Δ* sample. (C and D) Abundance and assembly the IFT-B and

changes in protein complexes, which can be quantified using novel statistical frameworks (Figure 1A, middle). We have demonstrated the utility of this technique for both the identification of RNA-binding proteins (Mallam *et al.*, 2019; Drew *et al.*, 2020) and phosphorylation-dependent protein–protein interactions (Floyd *et al.*, 2021). Here, we expand the utility of DIFFRAC to identify proteomic changes resulting from genetic mutation.

Importantly, DIFFRAC does not require genetic tagging or isotope labeling, making it, in principle, highly versatile and widely applicable. However, the method relies heavily on mass-spectrometry, with previous studies involving 250–350 individual mass spectrometry experiments (Mallam *et al.*, 2019; Drew *et al.*, 2020; Floyd *et al.*, 2021) .Developing workflow that minimizes instrument time and thus cost is an important goal. In addition, while DIFFRAC has been used successfully to compare drug-treated samples, the method is also theoretically suitable for comparison of proteome content between wild-type and genetic mutants. To explore these issues of utility, we used DIFFRAC to quantify the proteomic consequences of genetic loss of *Ift122*, a subunit of the Intraflagellar Transport-A (IFT-A) protein complex.

IFT is a deeply evolutionarily conserved process that is crucial for the formation and function of cilia and flagella. IFT proteins actively transport cargoes into and out of cilia by acting as adaptors between cargoes and the microtubule motors kinesin-II and IFT dynein (Walther *et al.*, 1994; Kozminski *et al.*, 1995; Cole, 1998; Pazour *et al.*, 1998, 1999; Porter, 1999; Signor, 1999). The IFT proteins form two distinct and highly conserved protein complexes, IFT-A and IFT-B (Sung and Leroux, 2013; Taschner and Lorentzen, 2016). Cargo transport of ciliary structural components, such as tubulin and outer dynein arms, by IFT-B is well-characterized (Ahmed, 2008; Bhogaraju, 2013; Kubo, 2016; Hou and Witman, 2017; Taschner, 2017; Dai, 2018). However, the role of IFT-A-mediated cargo transport is less well understood.

Within cilia, IFT-A is required for the movement of cargoes from the ciliary tip to the cell body (Piperno *et al.*, 1998; Iomini *et al.*, 2001, 2009; Tran *et al.*, 2008; Tsao and Gorovsky, 2008; Qin, 2011). IFT-A additionally mediates entry of membrane proteins from the cytoplasm to cilia through association with Tubby-like adaptors (Lee, 2008; Mukhopadhyay, 2010; Qin, 2011; Badgandi *et al.*, 2017; Hirano *et al.*, 2017; Picariello, 2019). Consequently, cilia of IFT-A mutants display tip accumulations of ciliary cargoes, altered membrane composition, and subsequent signal transduction defects (Lee, 2008; Mukhopadhyay, 2010; Qin, 2011; Badgandi *et al.*, 2017; Picariello, 2019). In addition to these roles in canonical trafficking of ciliary proteins, a growing body of research suggests that IFT-A also mediates trafficking outside of cilia. In particular, evidence links IFT-A to the trafficking of ciliary vesicles from the Golgi to the ciliary base (Fu, 2016; Quidwai *et al.*, 2021). The cargoes of this nonciliary IFT-A trafficking remain ill-defined.

Here, we compared the proteomes and interactomes of wild-type *Tetrahymena thermophila* and a previously established IFT-A-mutant strain (Tsao and Gorovsky, 2008). Quantification of these changes revealed that through even a single DIFFRAC experiment, known effects of IFT-A loss were robustly recapitulated. Crucially, the experiment also identified several novel IFT-A-regulated pro-

teins, many of which were validated using live imaging in *Xenopus* multiciliated cells (MCCs). These experiments demonstrate that the proteins identified by DIFFRAC provide insights into both ciliary and nonciliary functions of IFT-A. In addition, this work provides evidence that DIFFRAC workflow can minimize mass spectrometry instrument time while still providing valuable biological insight. Overall, we provide further evidence of the utility and versatility of DIFRRAC and provide new insights into IFT-A.

RESULTS AND DISCUSSION

DIFFRAC identifies changes in proteome organization in IFT-A-null *Tetrahymena*

To detect changes in proteomic organization caused by loss of IFT-A function, we performed DIFFRAC using control and *Ift122*-null (Tsao and Gorovsky, 2008) *Tetrahymena thermophila* (hereafter *Tetrahymena*) lines. We performed cofractionation mass spectrometry (CF/MS) on whole-cell protein extracts rather than isolated cilia to allow identification of both ciliary and nonciliary cargoes of IFT-A. Because CF/MS separates cell lysate via high-pressured liquid chromatography (HPLC) prior to protein identification, it has multiple advantages over traditional shotgun proteomic techniques. First, the separation results in many fractions that individually have fewer proteins, allowing for better detection of low abundance proteins via mass spectrometry. Additionally, the pattern of elution across fractions allows inference of each protein's higher-order organization within the cell (Havugimana *et al.*, 2012; Wan *et al.*, 2015; McWhite *et al.*, 2020; Sae-Lee *et al.*, 2022). Thus, CF/MS provides information on the abundance and interactions of observed proteins, while also improving observation of low abundance proteins.

Briefly, whole cells were lysed under nondenaturing conditions, and centrifugation was used to separate soluble protein complexes from axonemes and other aggregates. The method used was largely derived from protocols described in Gaertig *et al.* (2013), with the important caveat that cilia were *not* isolated from cell bodies prior to lysis. The resulting soluble fraction was further separated using size-exclusion HPLC to separate protein complexes by mass. Fractions were then analyzed by mass spectrometry to identify and quantify all proteins present in each fraction (Figure 1A, Supplemental Table S1; for link to raw data deposition in massIVE, see *Materials and Methods*). We then performed protein identification using MSBlender (Kwon *et al.*, 2011).

Because the UniProt *Tetrahymena* proteome is highly redundant and as yet only partially annotated, we utilized orthology mapping to create a "nonredundant" reference proteome. And, because we previously found that an "orthologue collapsed" version of the *Xenopus laevis* proteome boosted performance in comparative proteomics (Drew *et al.*, 2020; Lee *et al.*, 2020), we similarly collapsed the Uniprot *Tetrahymena* proteome. As detailed in the *Materials and Methods*, *Tetrahymena* proteins that map to the same eukaryotic ortholog group (orthogroup) via eggNOG (Huerta-Cepas *et al.*, 2019) were combined into a single entry such that each orthogroup entry contains every *Tetrahymena* paralogue predicted to have evolved from a common eukaryotic ancestral gene. These orthogroups can then be mapped to sets of human orthologues that share the same corresponding ancestral gene (Supplemental Table S1).

BBSome complexes are unaltered in the Ift122 mutant. For each complex, subunits coelute and do not have significantly altered abundance or elution patterns in the *Ift122Δ* sample. (E) The negative control CCT complex has consistent protein composition and abundance in the absence of *Ift122*. Individual complex members behave similarly in the two samples (compare black and blue line for CCT8) and subunits behave similarly to each other (compare black line of CCT8 to black line of CCT2, or blue line of CCT8 to blue line of CCT2).

UniProt *Tetrahymena* entries that do not map to an orthogroup are retained under their UniProt accession number in our reference proteome, as are members of orthogroups that are too large to collapse (see *Materials and Methods* for more information). For simplicity, individual entries in this collapsed proteome will henceforth be referred to as orthogroups.

This approach solves two major problems caused by the limited annotation of the *Tetrahymena* proteome: first, this proteome is moderately redundant, due to both genetic redundancy (Eisen *et al.*, 2006) and duplicate sequence database entries. Reducing this redundancy allows for more protein spectral matches when searching for peptides that uniquely identify proteins. Second, it allows us to identify the likely vertebrate orthologues of *Tetrahymena* proteins that would otherwise be unnamed.

We used the resulting protein identifications for qualitative analysis of select proteins by generating elution profiles. Elution profiles display the abundance of an individual protein across all collected fractions (Figure 1A), which allows for visual comparisons of a protein's separation "behavior" in the wild-type versus *Ift122Δ* samples. This analysis provides evidence for both how individual proteins behave and whether they form higher-order protein complexes (Figure 1A).

As a positive control for the method, we first examined the proteins of the IFT-A complex. In controls, the IFT-A proteins all strongly coeluted (Figure 1B, black), as expected for members of a stable protein complex. Previous studies in *Chlamydomonas* have shown that loss of a single IFT-A subunit results in a significant decrease in abundance of other IFT-A subunits, likely due to the destabilization and subsequent degradation of the unassembled proteins (Behal, 2012). Accordingly, DIFFRAC revealed a profound reduction of all observed IFT-A proteins in the Ift122 mutant (Figure 1B, blue).

As an initial negative control, we also examined a related ciliary protein complex, IFT-B, which previous work has shown is unaffected by IFT-A loss (Behal, 2012; Picariello, 2019). Reassuringly, the abundance and elution pattern of IFT-B subunits were essentially unchanged in the *Ift122Δ* sample (Figure 1C). This result shows that perturbation of complex assembly or stability upon loss of *Ift122* was specific to the IFT-A subcomplex.

As an additional negative control, we examined the CCT complex, a stable, highly conserved cytoplasmic chaperonin complex that, while present in *Tetrahymena* cilia (Seixas *et al.*, 2003), is not expected to be impacted by perturbation of IFT-A function. We observed coelution of distinct CCT subunits in controls, indicating the CCT complex was intact (Figure 1D, black), and the identical elution peaks in *Ift122* mutant samples demonstrate that the complex was unaffected (Figure 1D, blue). Together with the similar result for IFT-B, this result suggests that changes in elution of IFT-A complex subunits reflects a biological difference rather than denaturation of the sample during experimental preparation.

Finally, we examined several units of the ciliary BBSome complex, which acts an adapter between IFT-A and ciliary membrane proteins (Wingfield *et al.*, 2018). Interestingly, neither the abundance nor the behavior of the BBS proteins was appreciably altered in the *Ift122Δ* strain (Figure 1D), providing further evidence of the specificity of our IFT-A disruption. We note, however, that a previous proteomic study in *Chlamydomonas* (Picariello, 2019) found BBS proteins to be significantly increased in IFT-A null cilia, yet our results show unchanged abundance of an intact complex. While these data initially seem contradictory, a parsimonious explanation is that in the absence of IFT-A, the BBSome complex may still form, but the major population of this complex remains in the cell body rather than entering cilia.

Taken together, this qualitative analysis of elution profiles shows that the separation was successful. We next developed a pipeline to systematically identify proteins whose behavior or abundance differed between WT and *Ift122Δ* samples.

Detection of proteins significantly altered in *Ift122* mutants

To identify significantly changed protein orthogroups in *Ift122* mutants, we first estimated per-fraction z-scores and *p*-values (as described in (Floyd *et al.*, 2021)). Using a false discovery rate (FDR) cut-off of 0.1%, we identified a total of 617 orthogroups whose abundance or assembly state was significantly altered in *Ift122* null *Tetrahymena* (Supplemental Table S1). Crucially, IFT-A components represented the dominant outliers in this analysis (Figure 2A, blue text), while IFT-B components did not reach statistical significance (Figure 2A, gray text).

As a positive control, we looked for known IFT-A-related proteins in our dataset (Figure 2A, orange text). For example, previous work has shown that IFT-A/Tulp3 trafficking of Pkdh1 is required for its ciliary localization (Badgandi *et al.*, 2017). We observed a drastic decrease in Pkdh1 abundance in the *Ift122*-null strain (Figure 2B, upper), suggesting that nonciliary Pkdh1 may be either degraded or downregulated in *Ift122Δ*-mutant cells. Conversely, Cnga2 was previously observed to move along the olfactory sensory neuronal cilia in a manner indicative of IFT-dependent trafficking (Williams *et al.*, 2014), and its protein abundance is *increased* in the *Ift122* null strain, where the majority eluted at higher molecular weight that in wild type cells (Figure 2B, lower). As a membrane protein, it is likely that IFT-A regulates Cnga2 entry into the cilium as well as its subsequent retrograde movement. These data suggest that the quantitative analysis of our DIFFRAC data successfully identified proteins whose behavior is known to be altered in IFT mutants.

Our analysis also identified other known ciliary proteins linked previously to IFT. For example, the O-linked N-acetylglucosamine transferase OGT is essential for mammalian ciliogenesis (Yu *et al.*, 2020) and is elevated in the kidneys of mice with IFT-A-related ciliopathy (Wang *et al.*, 2022). Our finding that OGT abundance was significantly increase in IFT-A mutants in *Tetrahymena* (Figure 2A), suggests that the connection between IFT-A and OGT is conserved across eukaryotic cilia. Other ciliary proteins displayed similar profiles to Ogt, including Hydin, Cfap57, and Cfap46, while Pkhd1 displayed reciprocal changes (Figure 2A).

Also among the DIFFRAC hits were many proteins with known roles in protein synthesis, in particular, many subunits of the tRNA multisynthetase complex, translation elongation factors and ribosomal proteins (Supplemental Figure S2), These data suggest the possibility that IFT-A, like other ciliopathy proteins (Morleo *et al.*, 2022), may play a broader role in proteome regulation. These results encourage further study to determine whether IFT-A contributes to localized translation that has been proposed to occur either at basal bodies (Lerit, 2022) or within cilia (Hao *et al.*, 2021).

Finally, we performed an unbiased comparison of our results to other high-throughput studies seeking to identify putative ciliary genes or proteins (Hayes *et al.*, 2007; Chung *et al.*, 2014; Treutlein *et al.*, 2014; Quigley and Kintner, 2017; van Dam *et al.*, 2019; Sim *et al.*, 2020; May *et al.*, 2021). We observed an increased proportion of known ciliary proteins among the significantly changed proteins in *Ift122Δ* DIFFRAC (Figure 2C), although many other significantly changed proteins have not previously been identified or predicted to be ciliary. This class of proteins, which are significantly changed but do not have a known ciliary annotation, is likely composed of two types of proteins: 1) proteins that do in fact localize to the cilium, but have not yet been identified as such, or 2) proteins that do
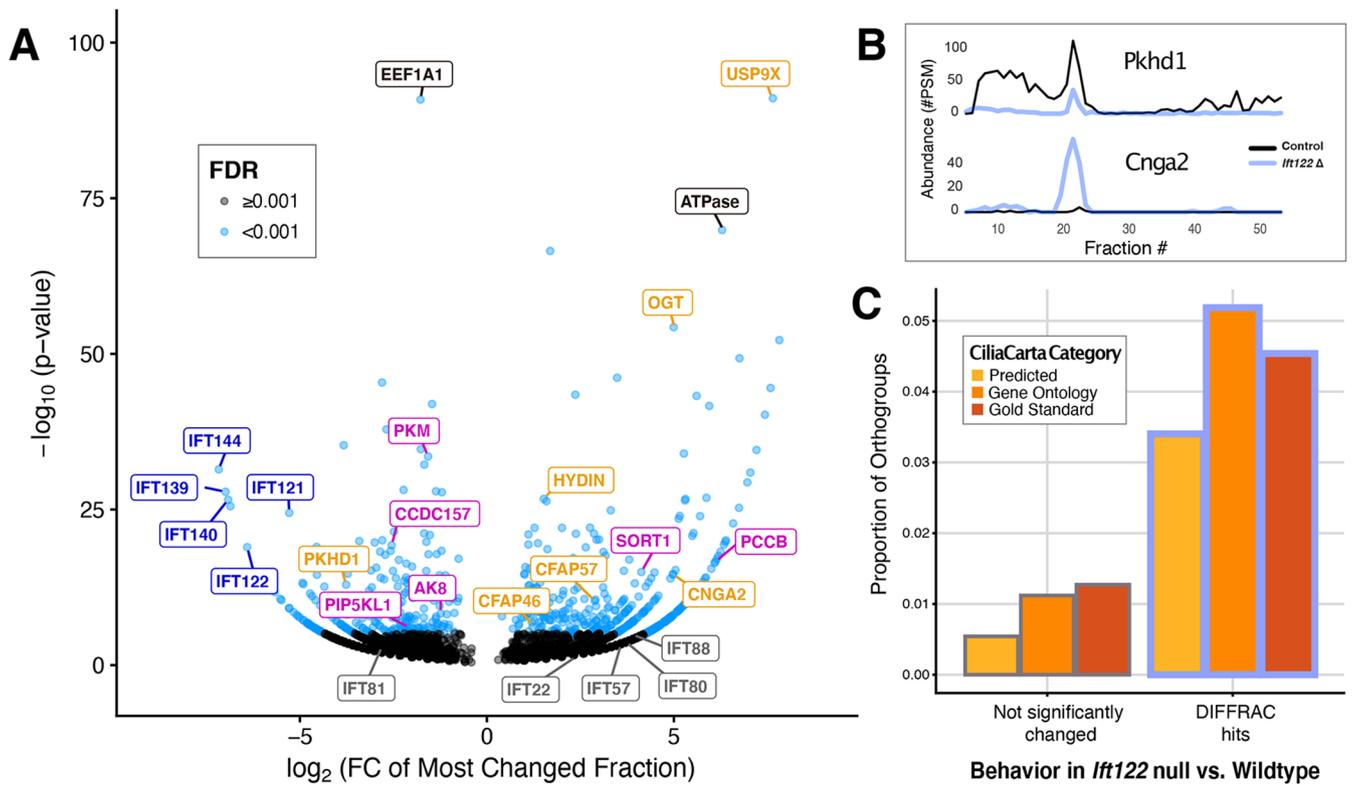
FIGURE 2: Differential abundance analysis identifies 617 orthogroups as significantly changed, including known IFT-A cargos. (A) Differential abundance of orthogroups in wild-type versus *Ift122Δ* proteomes. Plot of the fold change in abundance versus *p*-value for the maximum per fraction z-score calculated for every orthogroups observed in the experiment. Orthogroups that surpass the FDR = 0.001 (0.1%) cutoff are plotted as blue dots, while those that do not are plotted in gray. IFT-A orthogroups are labeled in dark blue, IFT-B orthogroups are labeled in gray, and known ciliary proteins are labeled in orange. Orthogroups corresponding to proteins further studied in this study are labeled in magenta. One of the highest significance orthogroups, ENOG502RZNF, does not have any predicted vertebrate homologues, but the *Tetrahymena* paralogues in this orthogroup are poorly characterized and are primarily annotated as putative ATPases. (B) Elution profiles of established IFT-A cargoes The known IFT-A cargo PKHD1 has reduced abundance in the *Ift122Δ* sample. In contrast, the orthogroups containing Cnga2 and OGT show increased abundance in the null strain. Additionally, Cnga2 elutes at higher molecular weight peak compared with the control sample, suggesting potential aggregation or accumulation of a larger protein complex. (C) Known and predicted ciliary proteins are enriched among DIFFRAC hits [OR] Coverage of known and predicted ciliary proteins among DIFFRAC hits Proportion of observed orthogroups that contain one or more vertebrate homologues identified by CiliaCarta as known or probable ciliary proteins. Categories are: "Gold Standard" proteins, for which significant experimental evidence of ciliary localization or function exists; "Gene Ontology" proteins which have previously been annotated with cilia-related GO-term; and proteins were "Predicted" to be ciliary using CiliaCarta's Bayesian model.

not localize to the cilium, but whose abundance, localization, or higher-order organization is dependent upon IFT-A function. A third possibility is proteins whose levels or localization are changed indirectly by the loss of *Ift122*, for example as a consequence of disrupted ciliary signaling. Given the complexity of unraveling the third possibility, we chose to further characterize a specific subset of proteins that appeared to fall into the first two categories (labeled in magenta in Figure 2A), selecting hits with a range of measured effect sizes in DIFFRAC.

Development of an *Ift122* knockdown model in *Xenopus*-motile cilia

We next sought to ask whether the proteomic changes observed by DIFFRAC in *Tetrahymena Ift122Δ* mutants would provide insights into the biology of vertebrate ciliated cells. To this end, we turned to *Xenopus* embryos, developing tools to deplete IFT122 and exploiting the large multiciliated cells for live imaging (Walentek and Quigley, 2017). We used antisense morpholino-

oligonucleotides (MOs) to disrupt splicing of the endogenous *Ift122* transcript, which via nonsense mediated decay reduces levels of *Ift122* mRNA (Figure 3A).

Genetic loss of IFT122 in *Tetrahymena*, *Chlamydomonas*, and mice is associated with a reduction in cilia number as well as reduced length in cila that remain (Tsao and Gorovsky, 2008; Cortellino *et al.*, 2009; Qin, 2011; Behal, 2012). We observed precisely these phenotypes in *Xenopus* MCCs after Knockdown (KD) of Ift122 (Figure 3, B and C). Indeed, by imaging the IFT-B subunit Ift46, even subtle aspects of the phenotype, such as enriched accumulation of Ift46 especially in the distal cilium, were recapitulated in our Ift122 morphants (Figure 3D). Finally, the gold standard control for off-target effects with MOs is rescue of the phenotype with nontargetable mRNA of the targeted gene (Blum *et al.*, 2015), and we confirmed that all phenotypes for Ift122 morphants were rescued by coinjection of Ift122 mRNA (Figure 3C, D). Thus, IFT122 KD in *Xenopus* provides an effective platform in which to assess defective IFT-A
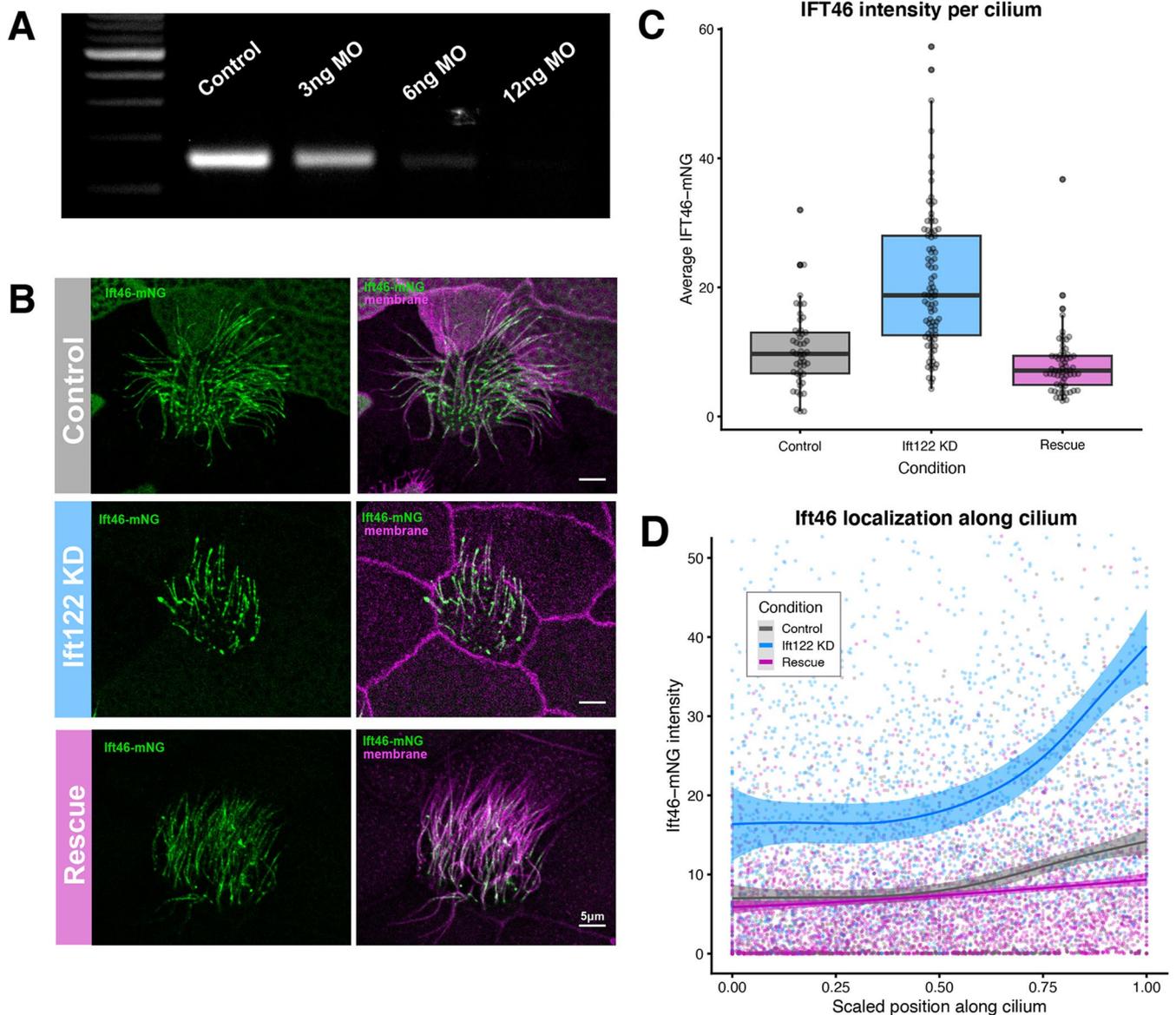
FIGURE 3: *Ift122* knockdown in *Xenopus* recapitulates evolutionarily conserved IFT-A loss of function phenotypes, which are rescued by *Ift122* overexpression. (A) RT-PCR validation of *Ift122* morpholino mediated knockdown. Dose curve of morpholino targeting the first splice junction of *Ift122* pre-mRNA. Embryos were injected at the four-cell stage and mRNA was extracted at stage 25. Subsequent RT-PCR amplification of the MO target region shows a dose-dependent decrease in *Ift122* transcript levels. Because the 6 ng dose resulted in a robust reduction of transcripts but not a decrease in embryo viability (which was observed for the 12 ng dose – data NS), 6 ng injections were used for all following experiments. (B–D) Increase in ciliary IFT-B localization and tip accumulation upon *Ift122* knockdown in epidermal MCC cilia. (B) Representative images of Ift46 ciliary localization in control, *Ift122* knockdown, and rescue embryos. Note loss of cilia numbers and accumulation of Ift46 in morphants of rescue of both phenotypes. All fusion constructs were injected as mRNAs. CAAX-RFP labels both cell and ciliary membrane, IFT-B is labeled with Ift46-mNG, and the phenotypes were rescued with the addition of Ift1222-FLAG mRNA. (C) The average intensity of Ift46-mNG per cilium is significantly increased upon MO-mediated knockdown of *Ift122*. This change is rescued by addition of Ift122-FLAG mRNA. (D) The tip accumulation of Ift46 in *Ift122* KD cilia is rescued by addition of Ift122-FLAG mRNA. 1 corresponds to the distal-most Ift46-mNG signal (toward the ciliary tip), 0 corresponds to the proximal-most point measured (toward the ciliary base). Points show the intensity of Ift46-mNG at a single, min-max scaled position along a single cilium. Min–max scaling was used for position normalization. Lines are smoothed conditional means calculated using locally estimated scatterplot smoothing (LOESS).

Tetrahymena DIFFRAC hits include ciliary exit and entry phenotypes upon Ift122 loss in *Xenopus*

Because IFT-A's most well-characterized function is in transport of proteins along the cilium, we first set our sights on DIFFRAC candidates with ciliary localization. IFT-A has been shown to control the exit of some cargoes from cilia (e.g., IFT-B) and the entry of other cargoes (e.g. membrane proteins such as Pkhd1, see Figure 2B). We were curious whether both ciliary-exit and ciliary-entry cargo were among our DIFFRAC hits, especially considering the inherent limitations of mass spectrometry observation of membrane proteins.

We first examined a known ciliary protein, Adenylate Kinase 8 (Ak8). Previous studies reported axonemal localization of Ak8 in sperm (Vadnais et al., 2014) and tracheal MCCs (Dougherty et al., 2020) and recent work suggest Ak8 is a component of radial spokes. We observed GFP-AK8 localization along the cilium in wild-type Xenopus MCCs as expected, but the signal was excluded from the distal-most region of cilia (Figure 4A), a pattern observed for most with axonemal structural or motility proteins (Lee et al., 2022).

We also found that Ak8 enrichment in cilia was significantly increased upon Ift122 knockdown (Figure 4, B and C), though unlike IFT-B, the increase in Ak8 intensity was consistent across the length of the cilium (Figure 4, A and C), rather than being enriched in the tip (Figure 3D). As retrograde IFT removes other radial spoke proteins from the axoneme (Qin, 2011) and IFT-A-mutant axonemes contain excess radial spoke proteins (Picariello, 2019), a parsimonious interpretation of these data would be that IFT-A regulates homeostatic removal of Ak8 from the axoneme. Alternatively, since cilia numbers are reduced, the result may instead reflect a set level of Ak8 being distributed across a smaller number of cilia in IFT-A morphants, a scenario that could inform recent findings of IFT-A-associated redistribution of ciliary proteins between individual axonemes in MCCs (Rao et al., 2023).

We next analyzed the impact of Ift122 KD on a novel ciliary protein, Pip5kl1. When first examining the DIFFRAC hits, we were intrigued to find the large orthogroup KOG0229 containing several phosphatidylinositol kinases (Figure 2A, magenta; Supplemental Table S1), as the distinctive phospholipid composition of the ciliary membrane is crucial for normal signaling and thus tightly regulated (Nechipurenko, 2020; Dutta and Ray, 2022). Of this relatively large orthogroup, Pip5kl1 was the only vertebrate paralogue that was also identified as a target of the Rfx2 ciliary transcriptional network (Chung et al., 2014; Quigley and Kintner, 2017), so we chose this protein for examination.

In our initial experiments, we found that Pip5kl1 robustly localizes to cilia of Xenopus MCCs (Figure 4E). Pip5kl1 is poorly characterized, but the few studies that have been performed show that while it lacks kinase activity, it regulates membrane phospholipid content by controlling the localization of other, enzymatically active PIP5Ks (Yang et al., 2019). Interestingly, Pip5kl1 localization extended to the full length of the cilium as marked by membrane-RFP, in contrast to AK8 (Figure 4, A and E) and other structure components of the axoneme. This suggests that Pip5kl1 may, like other proteins in the KOG0229 orthogroup, be membrane associated. Consistent with this idea, IFT-A controls the entry of many membrane proteins to cilia, and after Ift122 KD in Xenopus MCCs, Pip5kl1 was strongly depleted from MCC axonemes (Figure 4, E-G). Together, these data demonstrate that DIFFRAC of Ift122 mutants identified both entry and exit cargoes of IFT-A, reinforcing the utility of this method.

IFT-A is required for normal localization of Ccdc157 both within the axoneme and at the base of cilia

Among the most interesting proteins identified in Ift122 DIFFRAC was Ccdc157 (Figure 2A, magenta; Supplemental Table S1). This gene is implicated in spermatogenesis in Drosophila, and it is downregulated in human males with nonobstructive azoospermia (Yuan et al., 2019). Like IFT-A (Fu et al., 2016; Quidwai et al., 2021), Ccdc157 protein localizes to post-Golgi vesicles (Bassaganyas et al., 2019). Finally, Ccdc157 is strongly enriched in human tissues with motile cilia or flagella such as the testis and the fallopian tubes (Uhlén et al., 2015) and is a known direct target of the ciliary transcription factor Rfx2 in Xenopus (Chung et al., 2014). However, the localization of Ccdc157 in vertebrate ciliated cells has never been reported.

Interestingly, Ccdc157-GFP displayed consistent, robust localization at the base of cilia in MCCs (Figure 5A). Imaging together with Centrin-RFP revealed that Ccdc157 was not present at basal bodies, but rather was adjacent, in a polarized pattern indicative of cilia rootlet localization (Figure 5A, insets). Ccdc157 also displayed a weak but consistent ciliary localization that varied between individual cilia (Figure 5B); most cilia had no obvious GFP-Ccdc157 signal, some had modest localization, and a small minority had very intense signal.

Knockdown of Ift122 elicited an interesting change to the localization of Ccdc157. The localization at the ciliary base significantly decreased upon knockdown (Figure 5C), with no obvious accumulation of Ccdc157 elsewhere in the cell body (not shown). Instead, the ciliary localization of Ccdc157 increased significantly (Figure 5D). While the amount of axonemal Ccdc157 was still variable across individual cilia in the ift122 morphants, the average GFP-Ccdc157 intensity per cilium increased significantly. Interestingly, the relative localization levels of Ccdc157 were consistent along the length of cilium, similar to that observed for Ak8 but distinct from that of Ift46 after Ift122 KD. These data suggest that IFT-A controls the distribution of what seem to be two distinct pools of Ccdc157 in the axoneme and at the basal body.

DIFFRAC identifies nonciliary proteins altered by mutation of Ift122

In addition to known roles for ciliary entry and exit, an emerging literature has revealed a role for IFT-A in the cytoplasm, and IFT-A proteins localize not only to the axoneme, but also to robustly to a peri-basal body pool in Xenopus MCCs (Hibbard et al., 2021). Moreover, work in other systems suggests that IFT-A also acts at the Golgi (Fu et al., 2016; Quidwai et al., 2021). It is of interest, then, that Ift122 DIFFRAC also identified proteins with no ciliary localization.

Among these was Sort1, a well-characterized regulator of protein transport from the Golgi (Conlon, 2019) (Figure 2A; Supplemental Table S1). Although not known to regulate any aspect of ciliary biology, the Sort1 gene is a direct target of the ciliary transcription factor Rfx2 (Chung et al., 2014), so we examined its localization. In Xenopus MCCs, we found that Sort1 localizes not only to Golgi but also to puncta at the apical surface of the MCCs near the basal bodies (Supplemental Figure S3A). While these apical puncta are not specific to MCCs, they are more abundant in MCCs than other epidermal cell types, especially during ciliogenesis stages (not shown). Given the role of IFT-A in trafficking ciliary vesicles from the Golgi to the ciliary base, these data suggest that Sort1 may be an interesting candiate for further study.

The mitochondria-related pyruvate kinase Pkm was also identified as a DIFFRAC hit (Figure 2A, Supplemental Table S1), and this protein was previously identified in a proteomic analysis of Xenopus MCC axonemes (Sim et al., 2020), suggesting potential ciliary localization. Although this putative localization has not been confirmed with imaging experiments, and we did not observe Pkm-GFP to colocalize with cilia. Rather, Pkm localized in foci throughout the cell, but many of the more prominent foci were coincident with basal bodies (Supplemental Figure S3B).

Finally, another metabolism-related protein, the propionyl-CoA carboxylase subunit Pccb (Figure 2A; Supplemental Table S1) was also identified in our DIFFRAC. Pccb displayed a more overtly interesting localization, strongly concentrated in the apical cytoplasm, both in contact with basal body and in a reticulated network linking them (Figure 6A). Strikingly, this apical population of Pccb was severely depleted after Ift122 KD (Figure 6B), suggesting that IFT-A may play a role either in Pccb transport in the cytoplasm or in its capture at basal bodies.
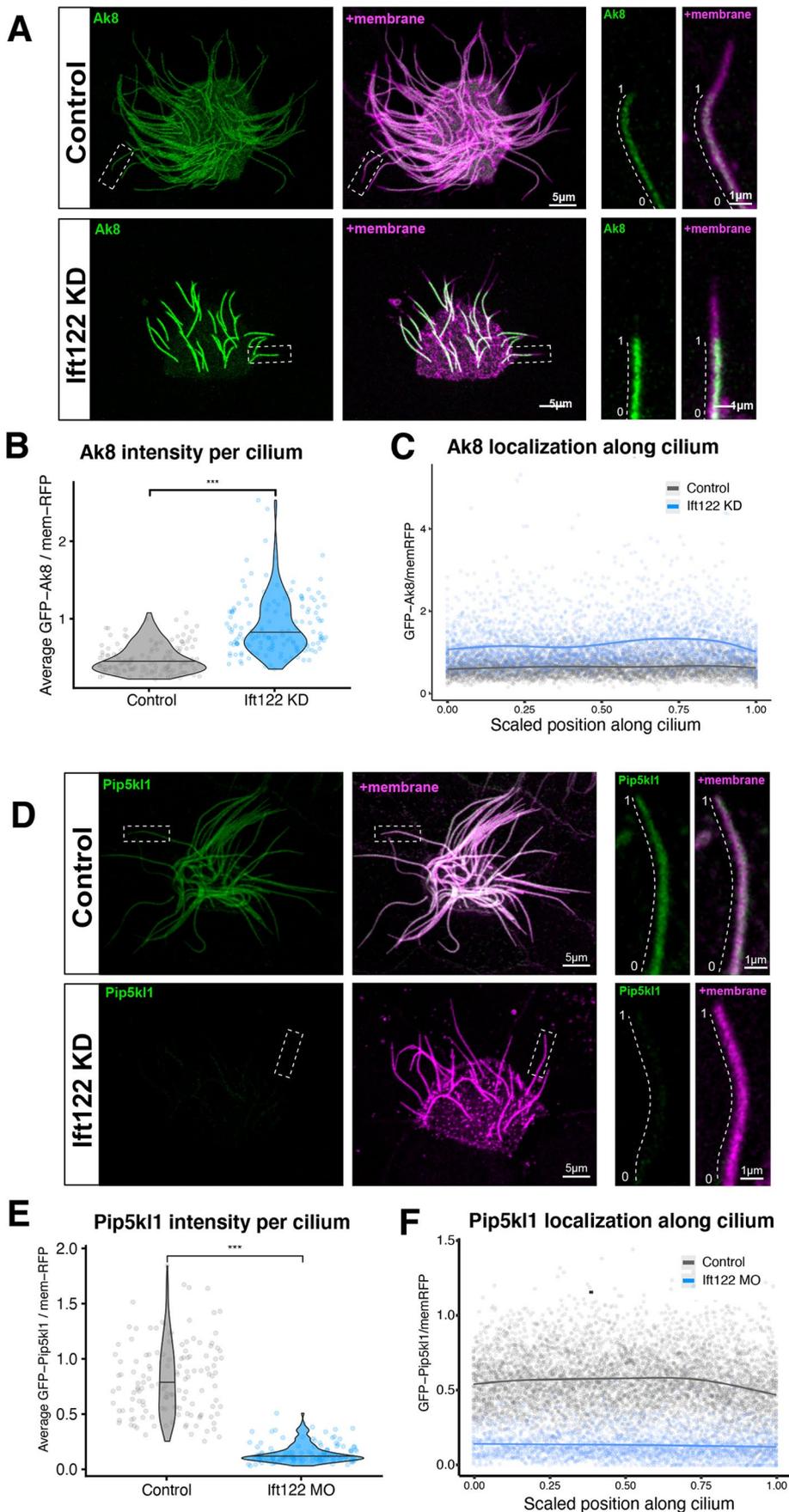
FIGURE 4: DIFFRAC identifies IFT-A-mediated ciliary exit and entry cargo. (A–C) Ak8 localization increases along the entire length Ift122 KD cilia, suggesting IFT-A is required for ciliary exit of Ak8. (A) Representative images. Membrane is labeled with CAAX-RFP, and Ak8 is visualized with a GFP-tagged construct. (B) The average GFP-Ak8 intensity/CAAX-RFP intensity per cilium increased from 0.492 ± 0.187 in control to 0.91 ± 0.377 in Ift122 KD (***$p < 0.001$, Wilcoxon rank sum test with continuity correction; Control, $n = 134$ cilia from 29 cells, $N = 6$; Ift122 KD, $n = 145$ cilia from 41 cells, $N = 6$). Data represent mean $\pm$ S.D. (C) Ak8-GFP intensity versus scaled position along cilium. In contrast to the tip accumulation of Ift46-mNG, the intensity of GFP-Ak8 increases evenly along the length of the cilium in the *Ift122* KD. (1) denotes the distal-most Ak8-GFP signal (toward the ciliary tip), (0) denotes the proximal-most point measured (toward the ciliary base). Points show the intensity of GFP-Ak8 at a single, min–max scaled position along a single cilium. Lines are smoothed conditional means calculated using a general additive model (GAM). The smoothed means are calculated from all data points, but points above the 99th percentile of GFP-Ak8 intensity are not shown. (D–F) Novel ciliary protein Pip5kl1 has increased ciliary localization upon *Ift122* KD, suggesting IFT-A regulates its entry into the cilium. (D) Representative images. Membrane is labeled with CAAX-RFP, and Pip5kl1 is visualized with an n-terminal GFP-tagged construct. GFP-Pip5kl1 localizes along the entirety of the ciliary membrane. (E) Quantification of average GFP-Pip5kl1 intensity per cilium. GFP-Pip5kl1/CAAX-RFP is reduced from 0.812 ± 0.33 in control to 0.147 ± 0.0864 in Ift122 KD (***$p < 0.001$, Wilcoxon rank sum test with continuity correction; Control, $n = 135$ cilia from 33 cells, $N = 6$; Ift122 KD, $n = 135$ cilia from 41 cells, $N = 7$). Data represent mean $\pm$ S.D. (F) Pip5kl1 localization along the cilium: GFP-Pip5kl1 intensity versus scaled position along the cilium. From proximal (0) to distal (1) in relation to the cell body. Points show the intensity of GFP-Pip5kl1 at a single, min–max scaled position along a single cilium. Lines are smoothed conditional means calculated using a GAM. The smoothed means are calculated from all data points, but points above the 99th percentile of GFP-Pip5kl1 intensity are not shown.
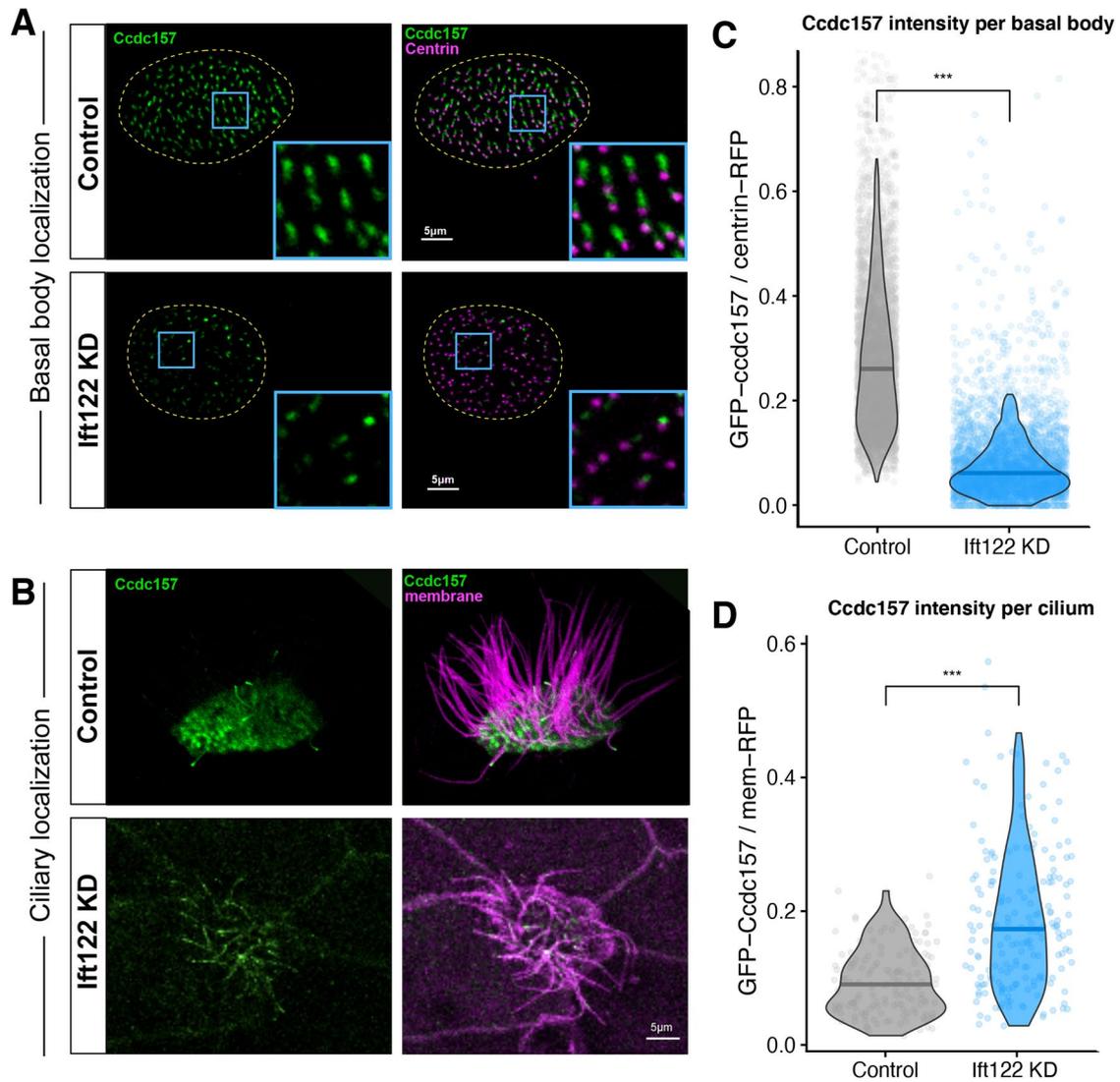
FIGURE 5: Ift122 regulates both the ciliary and subapical localization of novel ciliary protein Ccdc157.
(A and B) Ccdc157 displays variable ciliary localization that is significantly increased upon Ift122 knockdown.
(A) Representative images showing increased localization of GFP-Ccdc157 in Ift122 KD cilia. (B) Knockdown of Ift122 increases average GFP-Ccdc157/CAAX-RFP per cilium from 0.0957 ± 0.0503 in control to 0.196 ± 0.125 in Ift122 KD ($***p < 0.001$, Wilcoxon rank sum test with continuity correction; Control, $n = 155$ cilia from 34 cells, $N = 6$; Ift122 KD, $n = 191$ cilia from 41 cells, $N = 6$). Data represent mean±s.d. Statistics are calculated from all data points, but outliers are not shown. (C and D) Ccdc157 has robust peri-basal body localization in wildtype cells but is lost from this region in *Ift122* KD MCCs. (C) Representative images of the polarized, peri-basal body localization of GFP-Ccdc157. Basal bodies are labeled with centrin-RFP. Average intensity of GFP-Ccdc157 per basal body is significantly reduced in Ift122 KD MCCs, as quantified in (D). Means are calculated from all data points, but outliers are not shown. ($***P < 0.001$, Wilcoxon rank sum test with continuity correction; Control, $n = 4768$ basal bodies from 30 cells, $N = 6$; Ift122 KD, $n = 3820$ basal bodies from 30 cells, $N = 6$).

CONCLUSIONS

Here, we used DIFFRAC, a label-free method for assessing proteomic changes (Mallam *et al.*, 2019; Drew *et al.*, 2020; Floyd *et al.*, 2021), to examine the effect of IFT-A loss on the *Tetrahymena* proteome. Crucially, even a single DIFFRAC experiment in *Tetrahymena*, involving a relatively small number (102) of independent mass spectrometry experiments was sufficient to identify changes in protein behavior that recapitulate diverse known effects of IFT-A loss, and moreover discover new biology. Several of the findings were further validated using experiments in vertebrate embryos.

Using *Xenopus* MCCs, we show that the *Tetrahymena* DIFFRAC identified novel ciliary proteins, providing insights into both ciliary "exit" and "entry" functions of IFT-A. Foundational experiments

suggested a role for IFT-A in retrograde transport of IFT-B and other axonemal proteins (Rosenbaum and Witman, 2002). Accordingly, axonemal proteins such as Ak8 were significant hits in *Tethraymena* DIFFRAC and accumulated in cilia after Ift122 KD in *Xenopus*. Interestingly, Ak8 is thought to control ATP homeostasis and physically interacts with the axonemal protein Cfap45 (Owa *et al.*, 2019; Dougherty *et al.*, 2020), while another paper suggests it may also be a component of the radial spokes (Zhang *et al.*, 2022). These data suggest that like Ak8, other significantly changed axonemal proteins such as Cfap57 and Hydin (Figure 2A), may require IFT-A for their homeostatic removal from axonemes.

More recently, IFT-A was also shown to control the entry of membrane proteins into cilia (reviewed in (Wingfield *et al.*, 2018), and our
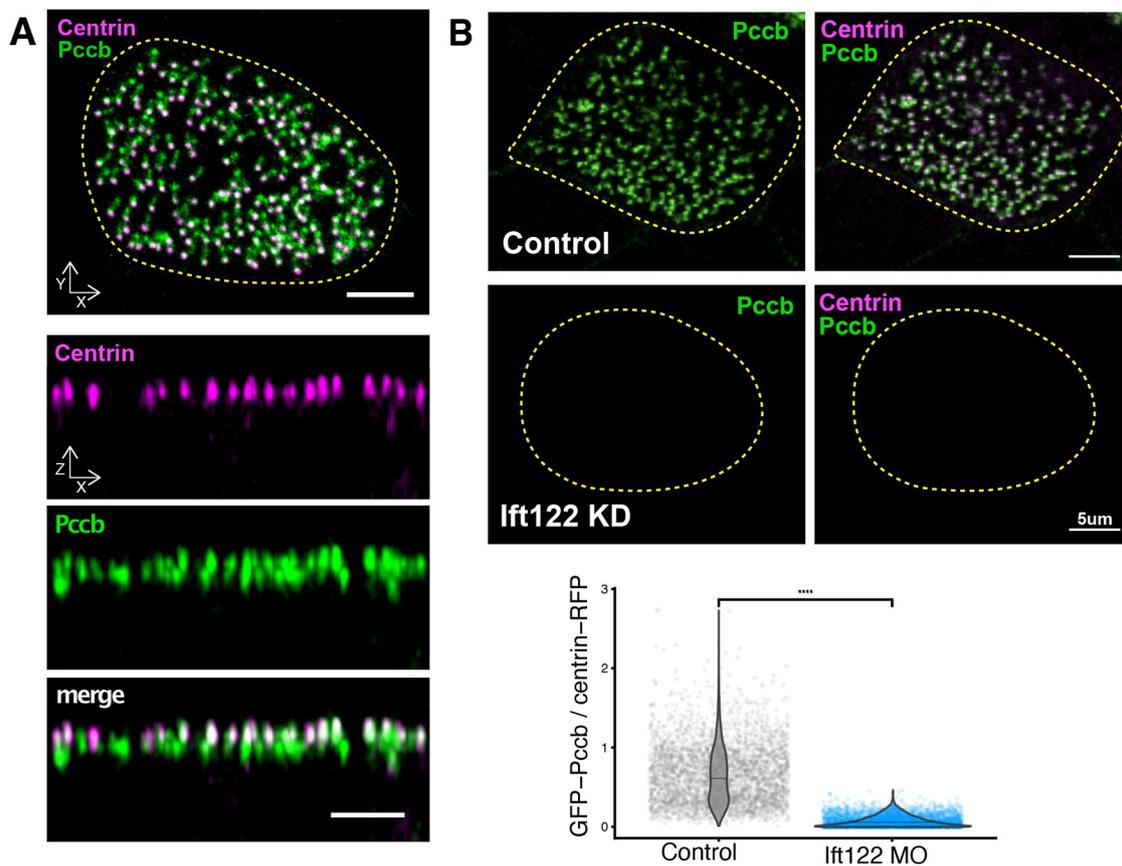
FIGURE 6: Pccb localization near basal bodies in Ift122-dependent. (A) Pccb-GFP (green) is enriched near basal bodies labeled by Centrin-RFP (magenta). Orthogonal views reveal Pccb is present at and below the position of the basal bodies. (B) Ift122 KD severely deplete GFP-Pccb intensity at basal bodies (marked by centrin-RFP) (***$p < 0.001$, Wilcoxon rank sum test with continuity correction; Control, $n = 3462$ basal bodies from 24 cells, $N = 4$; Ift122 KD, $n = 3540$ basal bodies from 24 cells, $N = 4$). Data represent mean $\pm$ s.d.

DIFFRAC provided insight into this function as well, identifying Pip5kl1 as a ciliary protein that requires IFT-A for entry. Finally, we revealed ciliary and basal body localization for poorly defined proteins such as Ccdc157 and proteins not previously implicated in cilia assembly or function, such as Pccb and Pkm.

Perhaps most intriguing among the DIFFRAC are those without known ciliary or basal body localization. One example is Sort1, which localized to the Golgi and apical puncta in MCCs (Figure 6A). Given Sort1's known roles in post-Golgi trafficking of diverse cargoes (Mitok *et al.*, 2022), this result raises the question of whether Sort1 regulates cargo-sorting or trafficking of IFT-A-coated vesicles to the ciliary base (Quidwai *et al.*, 2021).

In sum, our data show that even a simple DIFFRAC screen performed on a single biological replicate was sufficient to generate both biological insights and new hypotheses, despite the clear limitations to its implementation here. For example, the method could be improved by separately analyzing cell bodies and isolated cilia to better capture the localization of targets. Moreover, coupling the method to RNA-sequencing would enable us to better define direct versus indirect effects on the proteome. Nonetheless, the data presented here reinforce the utility of discovery-based proteomics for ciliary biology, even across large evolutionary distances such as that separating *Tetrahymena* and *Xenopus*.

MATERIALS AND METHODS
Request a protocol through *Bio-protocol.*

Tetrahymena strains and cultivation
WT (CU428, TSC_SD00178, Tetrahymena Stock Center) and ift122D (ift122D, heterokaryon cross of 5.3ns (TSC_SD01791) x 5.3s (TSC_SD01792); (Tsao and Gorovsky, 2008)). *Tetrahymena thermophila* cells were obtained from the Tetrahymena Stock Center. 3 L of *Tetrahymena thermophila* cells were grown to 1.9×10^5 and 3.4×10^5 cells/mL for CU428 and ift122D, respectively.

Tetrahymena protein extraction and fractionation
Nondenaturing conditions were used to extract stable protein complexes from whole-cell lysates of both the WT and *Ift122Δ*-mutant strains, which were then subjected to size-exclusion chromatography (SEC) fractionation and liquid chromatography tandem mass spectrometry (LC-MS/MS).

Cell collection. Cells were counted to ensure equivalent numbers of cells were used for each sample, despite the lower confluence of the *Ift122Δ* strain. A total of approximately 8×10^7 live, whole cells (per sample) were pelleted via centrifugation at $1700 \times g$ (JA 20 rotor, Beckman Coulter Inc, Brea, CA) for 10 min at room temperature. The resulting cell pellet was resuspended in 10 mM Tris-HCl pH 7.5 and washed by centrifugation.

Cell lysis. The cell pellet was frozen in a liquid nitrogen bath and ground using a mortar and pestle. The resulting powder was further lysed via resuspension in "Whole-Cell Lysis Buffer": 50 mM Tris-HCl

pH 7.4,, 1% NP40, 50 mM NaCl, 3 mM MgSO$_4$, 0.1 mM EGTA, 250 mM sucrose, 1 mM DTT (modified from Cilia Wash Buffer in [Gaertig *et al.*, 2013]) containing the following inhibitors: 1x cOmplete mini EDTA-free protease inhibitors (Roche), 1x PhosSTOP EASY phosphatase inhibitor (Roche), and 0.1 mM PMSF. All subsequent steps were performed at 4°C.

Protein extraction. Insoluble material and unlysed cells were pelleted by centrifugation at $3000 \times g$ for 10 min. The resulting supernatant was then centrifuged at $45,000 \times g$ for 10 min to further remove axonemes. The supernatant was then clarified by ultracentrifugation at $130,000 \times g$ for 1 h. The resulting high-speed supernatant contained soluble protein complexes. This soluble fraction (referred to as "protein extract" elsewhere) was used for subsequent proteomic analysis.

Size-exclusion chromatography. Both control and *Ift122Δ* protein extracts were subjected to size-exclusion chromatography independently using an UltiMate 3000 HPLC system (Thermo Fisher Scientific, Waltham, MA). Filtered soluble protein extract (0.45 μM; 2 mg total, 200 μl at 10 mg/ml) was applied to a BioSep-SEC-s4000 600 7.8 mm ID, particle diameter 5 μm, pore diameter 500 Å (Phenomenex, Torrance, CA) and equilibrated at a flow rate of 0.5 ml/min in "Buffer S-C": 50 mM Tris-HCl pH 7.4, 50 mM NaCl, 3 mM MgSO$_4$, 0.1 mM EGTA. A total of 67 fractions of 375 μl were collected, but only fractions with a robust A280 signal (fractions 4–54) were prepared for mass spectrometry.

The above protocol was first performed using the wild-type (CU428) sample. Once the resulting protein extract had been loaded onto the HPLC for fractionation, the protocol was repeated for the *Ift122Δ* strain. Fractionation of the *Ift122Δ* protein extract was also performed immediately after preparation.

Proteomic Analysis

Mass spectrometry. Fractions were concentrated by ultrafiltration with a 10 kDa molecular weight cut-off to 50 μl, denatured, and reduced in 50% 2,2,2-trifluoroethanol (TFE) and 5 mM tris(2-carboxyethyl)phosphine (TCEP) at 55°C for 45 min, and alkylated in the dark with iodoacetamide (55 mM, 30 min, room temperature). Iodoacetamide was then quenched with DTT. Samples were diluted to 5% TFE in 50 mM Tris-HCl, pH 8.0, 2 mM CaCl$_2$, and digested with trypsin (1:50; proteomics grade; 5 h; 37°C). Digestion was quenched (1% formic acid), and the sample volume reduced to 100 μl by speed vacuum centrifugation. The sample was desalted on a C18 filter plate (Part No. MFNSC18.10 Glygen Corp, Columbia, MD), eluted, reduced to near dryness by speed vacuum centrifugation, and resuspended in 5% acetonitrile/0.1% formic acid for analysis by LC-MS/MS. Peptides were separated on a 75 μM × 25 cm Acclaim PepMap100 C-18 column (Thermo Fisher Scientific) using a 3–45% acetonitrile gradient over 60 min and analyzed online by nanoelectrospray-ionization tandem mass spectrometry on an Orbitrap Fusion (Thermo Scientific).

The raw mass spectrometry data have been deposited in massIVE and can be accessed using FTP download link: ftp://MSV000091472@massive.ucsd.edu (Username: MSV000091472_reviewer; Password: a)

Reference proteome construction. We created a "nonredundant" reference proteome for interpreting mass spectrometry data based on the UniProt *Tetrahymena thermophila* reference proteome (proteome ID: U000009168). This improved protein identification performance by collapsing duplicated genes (Eisen *et al.*, 2006) and redundant Uniprot annotations. Specifically, we collapsed the UniProt reference proteome into protein families as assigned by the EggNOG eukaryote-level (euNOG) v5.0 mapping (Huerta-Cepas *et al.*, 2019), calculated as described previously (Drew *et al.*, 2020; Lee *et al.*, 2020). To avoid errors that arise when running MSBlender with proteomes that contain exceptionally large entries, an entry "length-limit" was applied – for example, the collapse was limited to orthogroups that, when combined, have a length less than 100,000 amino acids. *Tetrahymena* proteins that do not map to an euNOG5 group or are members of orthogroups that surpass this length limit are retained in the reference proteome and identified by their UniProt accession number.

Protein identification. RAW datafiles files were first converted to mzXML file format using MSConvert (http://proteowizard.source-forge.net/tools.shtml) and then processed using the MSBlender protein identification pipeline (Kwon *et al.*, 2011), combining peptide-spectral matching scores from MSGFþ (Kim and Pevzner, 2014), X! TANDEM (Craig and Beavis, 2004), and Comet (Lingner *et al.*, 2011) as peptide search engines with default settings. A FDR of 1% was used for peptide identification. Elution profiles were assembled using unique peptide spectral matches for each eggNOG orthogroup across all fractions collected.

Differential abundance calculations. To identify orthogroups that displayed significantly changed elution profiles, we compared the number of peptide spectrum matches (PSMs) between the control and the *Ift122Δ* samples in each fraction. The per fraction PSM counts were compared across all elution profiles to estimate z-scores, as described previously (Floyd *et al.*, 2021). From these z-scores, *p*-values and FDRs were calculated, correcting for multiple hypothesis testing using the Benjamini-Hochberg procedure (Benjamini and Hochberg, 1995). We considered any orthogroup with an FDR < 0.001 (0.1%) to be significantly changed.

Plasmids and cloning

The following constructs have been previously described: Mito-RFP, Lifeact-RFP, pCS-Centrin4-BFP and CAAX-RFP (Tu *et al.*, 2018), pCS-Centrin4-RFP (Park *et al.*, 2008), and pCS2-Ift46-mNG (Hibbard, 2021).

The GFP-Pkm expression construct contains the Pkm.S coding sequence obtained from DNASU (Seiler *et al.*, 2014) in a modified CS10R vector containing a GFP tag and the *tuba4* promotor (Tu *et al.*, 2018)). Gateway recombination was performed using Gateway LR Clonase II Enzyme mix (Thermo Fisher Scientific).

For all other new *Xenopus laevis* constructs, gene sequences were obtained from Xenbase (www.xenbase.org) (Karimi *et al.*, 2018). Open-reading frames were amplified from a *Xenopus* cDNA library by polymerase chain reaction. ORFs were inserted into the CS10R MCC vector. This vector contains a fluorescent tag with both SP6 and *tuba4* promotors, thus allowing either in vitro transcription of expression mRNAs or in vivo, MCC-specific expression of the fusion protein.

All constructs were verified by sequencing.

Xenopus embryo manipulations

Follow-up experiments on select candidates were performed in *Xenopus laevis*. All *Xenopus* experiments were conducted in accordance with the animal protocol AUP-2018-00225 and the animal ethics guidelines of the University of Texas at Austin.

To induce ovulation, female adult *Xenopus laevis* were injected with human chorionic gonadotropin the night preceding experiments. Females were squeezed to lay eggs, and eggs were fertilized

in vitro with homogenized testis. Two-cell stage embryos were dejellied in 1/3X Marc's modified Ringer's (MMR) with 3% (wt/vol) cysteine (pH 7.9), then washed and maintained in 1/3X MMR solution until the appropriate stage. For plasmid, mRNA, or CRISPR microinjections, embryos were placed in 2% Ficoll in 1/3X MMR and injected using a glass needle, forceps, and an Oxford universal micromanipulator.

Plasmid, mRNA, and MO microinjections

Pkm localization was visualized using injection of plasmid DNA (at 25 pg per blastomere) of the construct described above. mRNA injection was used for visualization all other fusion proteins (Ift46, Ak8, Pip5kl1, Ccdc157, Sort1, and Pccb).

Vectors for mRNA expression were linearized by restriction digestion and capped mRNAs were synthesized using the mMESSAGE mMACHINE SP6 transcription kit (Thermo Fisher Scientific, #AM1340).

Xenopus embryos were injected for candidate gene expression with mRNAs in the two ventral blastomeres at the four-cell stage to target the epidermis. Candidate mRNAs were injected at 100 pg per blastomere. Marker mRNAs were injected at 70–100 pg per blastomere (Centrin-BFP = 100 pg, Centrin-RFP = 100 pg, CAAX-RFP = 70 pg).

Ift122 MO was designed to target the exon1-intron2 splice junction. (Gene Tools, Philomath, OR). The MO sequence was 5'–AAAA-CTTGAAATCCTCTCACCTCTG–3' and the working concentration was 6 ng.

RT-PCR. To validate the efficacy of the Ift122 MO, embryos were injected with MO in all cells at the four-cell stage. Total RNA was extracted at stage 25 using TRIZOL (Invitrogen, Carlsbad, CA) and pooled from four embryos per condition. cDNA was prepared using the M-MLV Reverse Transcriptase (Invitrogen, Carlsbad, CA) kit and random hexamers. Ift122 cDNAs were amplified using GoTaq Green (Promega, Madison, WI) and the primers: fwd 5'-GGCAGCGGGTAGAGAGAATA-3' and rev 5'-GCACTC-TATTTCCTGCAGCC-3'.

Live imaging and image analysis

For live imaging, *Xenopus* embryos (stage 25–30) were mounted between two coverslips and submerged in 0.3X MMR and imaged on a Zeiss LSM700 confocal microscope using a or Plan-Apochromat 63 × 1.4 NA oil DIC M27 immersion lens. Each experiment includes multiple biological replicates, conducted on different days. Data for Ak8, Pip5kl1, and Ccdc157 localization experiments all include three replicates, while the Ift46 localization data represent two replicates. Three replicates were performed for Pccb localization, and all showed the same striking phenotype. Only data from one replicate (n = 4 per condition) was quantified (Figure 6E).

Images were processed using the Fiji distribution of ImageJ (Schindelin *et al.*, 2012) and figures were assembled in Illustrator (Adobe).

Quantification of fluorescence intensity of ciliary protein localization was performed on micrographs taken at the single z depth that best captured the length of the cilium. Regions of interest (ROIs) were manually drawn from the tip of each cilium to either just above the cell surface or as far as the individual cilium could be distinguished (and was not obscured by other cilia). ROIs were drawn using signal from Ift46-mNG, GFP-Pip5kl1, or GFP-Ak8 for respective experiments; however, the ciliary membrane CAAX-RFP signal was used to draw ROIs for GFP-Ccdc157 ciliary localization. Because there was wide variability in the intensity of GFP-Ccdc157 observed

across individual cilia, ROIs were drawn in the RFP channel to minimize bias in choice of cilia measured.

Quantification of fluorescence intensity of basal body localizing proteins was performed on micrographs taken at the single z depth which best captured the most basal bodies as labeled by centrin-RFP. Quantification performed on a subset of data using the maximum projection of z-stacks spanning the whole depth of the basal body region produced very similar results (data not shown). Due to increased imaging ease and speed, single z micrographs were used to analyze the whole datasets for both Pccb and Ccdc157 basal body localization data.

Fluorescence intensity was measured by first using the "Find Maxima" function in the centrin-RFP channel to automatically select basal bodies. ROIs were created using the "Extra-large" selection of the "Point Tool" function to create circles centered at the brightest points of RFP fluorescence. Measurements were then taken for the GFP-tagged candidate protein and centrin-RFP independently using the "Measure" function. Normalization was performed by calculating the ratio of candidate GFP intensity to the centrin-RFP intensity.

All statistical analyses and data visualization were performed using R (Vienna, Austria) and RStudio (Boston, MA). All relevant code can be found on GitHub at https://github.com/JLeggere/Ift122_DIFFRAC

REFERENCES

Ahmed NT (2008). ODA16 aids axonemal outer row dynein assembly through an interaction with the intraflagellar transport machinery. J Cell Biol 183, 313–322.

Badgandi HB, Hwang S, Shimada IS, Loriot E, Mukhopadhyay S (2017). Tubby family proteins are adapters for ciliary trafficking of integral membrane proteins. J Cell Biol 216, 743–760.

Bassaganyas L, Popa SJ, Horlbeck M, Puri C, Stewart SE, Campelo F, Ashok A, Butnaru CM, Brouwers N, Heydari K, *et al.* (2019). New factors for protein transport identified by a genome-wide CRISPRi screen in mammalian cells. J Cell Biol 218, 3861–3879.

Behal RH (2012). Subunit interactions and organization of the Chlamydomonas reinhardtii intraflagellar transport complex A proteins. J Biol Chem 287, 11689–11703.

Benjamini Y, Hochberg Y (1995). Controlling the false discovery rate: a practical and powerful approach to multiple testing. J Roy Stat Soc Ser B (Methodological) 57, 289–300.

Bertling E, *et al.* (2021). Carbonic anhydrase seven bundles filamentous actin and regulates dendritic spine morphology and density. EMBO Rep 22 e50145.

Bhogaraju S, Cajanek L, Fort C, Blisnick T, Weber K, Taschner M, Mizuno N, Lamla S, Bastin P, Nigg EA, Lorentzen E (2013). Molecular basis of tubulin transport within the cilium by IFT74 and IFT81. Science 341, 1009–1012.

Bludau I (2021). Discovery–versus hypothesis–driven detection of protein–protein interactions and complexes. I J Mol Sci 22, 4450.

Blum M, De Robertis EM, Wallingford JB, Niehrs C (2015). Morpholinos: antisense and sensibility. Dev Cell 35, 145–149.

Chung M-I, Kwon T, Tu F, Brooks ER, Gupta R, Meyer M, Baker JC, Marcotte EM, Wallingford JB (2014). Coordinated genomic control of ciliogenesis and cell movement by RFX2. eLife 3, e01439.

Cole DG (1998). Chlamydomonas kinesin-II-dependent intraflagellar transport (IFT): IFT particles contain proteins required for ciliary assembly in Caenorhabditis elegans sensory neurons. J Cell Biol 141, 993–1008.

Conlon DM (2019). Role of sortilin in lipid metabolism. Curr Opin Lipidol 30, 198–204.

Cortellino S, Wang C, Wang B, Bassi MR, Caretti E, Champeval D, Calmont A, Jarnik M, Burch J, Zaret KS, *et al.* (2009). Defective ciliogenesis, embryonic lethality and severe impairment of the Sonic Hedgehog pathway caused by inactivation of the mouse complex A intraflagellar

transport gene Ift122/Wdr10, partially overlapping with the DNA repair gene Med1/Mbd4. Developmental Biology 325, 225–237.

Dai J (2018). In vivo analysis of outer arm dynein transport reveals cargo-specific intraflagellar transport properties. Mol Biol Cell 29, 2553–2565.

Dougherty GW, Mizuno K, Nöthe-Menchen T, Ikawa Y, Boldt K, Ta-Shma A, Aprea I, Minegishi K, Pang Y-P, Pennekamp P, et al. (2020). CFAP45 deficiency causes situs abnormalities and asthenospermia by disrupting an axonemal adenine nucleotide homeostasis module. Nat Commun 11, 5520.

Drew K, Lee C, Cox RM, Dang V, Devitt CC, McWhite CD, Papoulas O, Huizar RL, Marcotte EM, Wallingford JB (2020). A systematic, label-free method for identifying RNA-associated proteins in vivo provides insights into vertebrate ciliary beating machinery. Dev Biol 467, 108–117.

Dutta P, Ray K (2022). Ciliary membrane, localised lipid modification and cilia function. J Cell Physiol 237, 2613–2631.

Eisen JA, Coyne RS, Wu M, Wu D, Thiagarajan M, Wortman JR, Badger JH, Ren Q, Amedeo P, Jones KM, et al. (2006). Macronuclear genome sequence of the ciliate Tetrahymena thermophila, a model eukaryote. PLoS Biology 4, e286.

Floyd BM, Drew K, Marcotte EM (2021). Systematic identification of protein phosphorylation-mediated interactions. J Proteome Res 20, 1359–1370.

Fu W, Wang L, Kim S, Li J, Dynlacht BD (2016). Role for the IFT-A complex in selective transport to the primary cilium. Cell Rep 17, 1505–1517.

Gaertig J, Wloga D, Vasudevan KK, Guha M, Dentler W (2013). Chapter thirteen - discovery and functional evaluation of ciliary proteins in Tetrahymena thermophila. In: Methods in Enzymology, ed. Marshall WF, Academic Press, 265–284.

Gingras A-C, Abe KT, Raught B (2019). Getting to know the neighborhood: using proximity-dependent biotinylation to characterize protein complexes and map organelles. Curr Opin Chem Biol 48, 44–54.

Hao K, Chen Y, Yan X, Zhu X (2021). Cilia locally synthesize proteins to sustain their ultrastructure and functions. Nat Commun 12, 6971.

Havugimana PC, Hart GT, Nepusz T, Yang H, Turinsky AL, Li Z, Wang PI, Boutz DR, Fong V, Phanse S, et al. (2012). A census of human soluble protein complexes. Cell 150, 1068–1081.

Hayes JM, Kim SK, Abitua PB, Park TJ, Herrington ER, Kitayama A, Grow MW, Ueno N, Wallingford JB (2007). Identification of novel ciliogenesis factors using a new in vivo model for mucociliary epithelial development. Developmental Biology 312, 115–130.

Hibbard JV (2021). Protein turnover dynamics suggest a diffusion-to-capture mechanism for peri-basal body recruitment and retention of intraflagellar transport proteins. Mol Biol Cell, 20–11–0717.

Hirano T, Katoh Y, Nakayama K (2017). Intraflagellar transport-A complex mediates ciliary entry and retrograde trafficking of ciliary G protein–coupled receptors. Mol Biol Cell 28, 429–439.

Hou Y, Witman GB (2017). The N-terminus of IFT46 mediates intraflagellar transport of outer arm dynein and its cargo-adaptor ODA16. Mol Biol Cell 28, 2420–2433.

Huerta-Cepas J, Szklarczyk D, Heller D, Hernández-Plaza A, Forslund SK, Cook H, Mende DR, Letunic I, Rattei T, Jensen LJ, et al. (2019). eggNOG 5.0: a hierarchical, functionally and phylogenetically annotated orthology resource based on 5090 organisms and 2502 viruses. Nucleic Acids Res 47, D309–D314.

Iomini C, Babaev-Khaimov V, Sassaroli M, Piperno G (2001). Protein particles in Chlamydomonas flagella undergo a transport cycle consisting of four phases. J Cell Biol 153, 13–24.

Iomini C, Li L, Esparza JM, Dutcher SK (2009). Retrograde intraflagellar transport mutants identify complex A proteins with multiple genetic interactions in Chlamydomonas reinhardtii. Genetics 183, 885–896.

Karimi K, Fortriede JD, Lotay VS, Burns KA, Wang DZ, Fisher ME, Pells TJ, James-Zorn C, Wang Y, Ponferrada VG, et al. (2018). Xenbase: a genomic, epigenomic and transcriptomic model organism database. Nucleic acids research 46, D861–D868.

Kozminski KG, Beech PL, Rosenbaum JL (1995). The Chlamydomonas kinesin-like protein FLA10 is involved in motility associated with the flagellar membrane. The Journal of Cell Biology 131, 1517–1527.

Kubo T (2016). Together, the IFT81 and IFT74 N-termini form the main module for intraflagellar transport of tubulin. J Cell Sci 129, 2106–2119.

Kwon T, Choi H, Vogel C, Nesvizhskii AI, Marcotte EM (2011). MSblender: A probabilistic approach for integrating peptide identifications from multiple database search engines. J Proteome Res 10, 2949–2958.

Lee C, Cox RM, Papoulas O, Horani A, Drew K, Devitt CC, Brody SL, Marcotte EM, Wallingford JB (2020). Functional partitioning of a liquid-like organelle during assembly of axonemal dyneins. eLife 9, e58662.

Lee C, Ma Y, Tu F, Wallingford JB (2023). Ordered deployment of distinct ciliary beating machines in growing axonemes of vertebrate multiciliated cells. Differentiation 131, 49–58.

Lee E (2008). An IFT-A protein is required to delimit functionally distinct zones in mechanosensory cilia. Curr Biol 18, 1899–1906.

Lerit DA (2022). Signed, sealed, and delivered: RNA localization and translation at centrosomes. MBoC 33, pe3.

Low TY, Syafruddin SE, Mohtar MA, Vellaichamy A, Rahman NSA, Pung Y-F, Tan CSH (2021). Recent progress in mass spectrometry-based strategies for elucidating protein–protein interactions. Cell Mol Life Sci 78, 5325–5339.

Mallam AL, Sae-Lee W, Schaub JM, Tu F, Battenhouse A, Jang YJ, Kim J, Wallingford JB, Finkelstein IJ, Marcotte EM, Drew K (2019). Systematic discovery of endogenous human ribonucleoprotein complexes. Cell Rep 29, 1351–1368.e5.

May EA, Kalocsay M, D'Auriac IG, Schuster PS, Gygi SP, Nachury MV, Mick DU (2021). Time-resolved proteomics profiling of the ciliary Hedgehog response. J Cell Biol 220, e202007207.

McWhite CD, Papoulas O, Drew K, Cox RM, June V, Dong OX, Kwon T, Wan C, Salmi ML, Roux SJ, et al. (2020). A Pan-plant protein complex map reveals deep conservation and novel assemblies. Cell 181, 460–474.e14.

Mitok KA, Keller MP, Attie AD (2022). Sorting through the extensive and confusing roles of sortilin in metabolic disease. J Lipid Res 63, 100243.

Monti C, Zilocchi M, Colugnat I, Alberio T (2019). Proteomics turns functional. J Proteomics 198, 36–44.

Morleo M, Pezzella N, Franco B (2022). Proteome balance in ciliopathies: the OFD1 protein example. Trends Mol Med 29, 201–217.

Mukhopadhyay S (2010). TULP3 bridges the IFT-A complex and membrane phosphoinositides to promote trafficking of G protein-coupled receptors into primary cilia. Genes Dev 24, 2180–2193.

Nechipurenko IV (2020). The enigmatic role of lipids in cilia signaling. Front Cell Dev Biol 8, 777.

Owa M, Uchihashi T, Yanagisawa H, Yamano T, Iguchi H, Fukuzawa H, Wakabayashi K, Ando T, Kikkawa M (2019). Inner lumen proteins stabilize doublet microtubules in cilia and flagella. Nat Commun 10, 1143.

Park TJ, Mitchell BJ, Abitua PB, Kintner C, Wallingford JB (2008). Dishevelled controls apical docking and planar polarization of basal bodies in ciliated epithelial cells. Nat Genet 40, 871–879.

Pazour GJ, Dickert BL, Witman GB (1999). The DHC1b (DHC2) isoform of cytoplasmic dynein is required for flagellar assembly. J Cell Biol 144, 473–481.

Pazour GJ, Wilkerson CG, Witman GB (1998). A dynein light chain is essential for the retrograde particle movement of intraflagellar transport (IFT. J Cell Biol 141, 979–992.

Picariello T (2019). A global analysis of IFT-A function reveals specialization for transport of membrane-associated proteins into cilia. J Cell Sci 132, jcs220749.

Piperno G, Siuda E, Henderson S, Segil M, Vaananen H, Sassaroli M (1998). Distinct mutants of retrograde intraflagellar transport (IFT) share similar morphological and molecular defects. J Cell Biol 143, 1591–1601.

Porter ME (1999). Cytoplasmic dynein heavy chain 1b is required for flagellar assembly in Chlamydomonas. Mol Biol Cell 10, 693–712.

Qin J (2011). Intraflagellar transport protein 122 antagonizes Sonic Hedgehog signaling and controls ciliary localization of pathway components. Proc Natl Acad Sci USA 108, 1456–1461.

Quidwai T, Wang J, Hall EA, Petriman NA, Leng W, Kiesel P, Wells JN, Murphy LC, Keighren MA, Marsh JA, et al. (2021). A WDR35-dependent coat protein complex transports ciliary membrane cargo vesicles to cilia. eLife 10, e69786.

Quigley IK, Kintner C (2017). Rfx2 stabilizes Foxj1 binding at chromatin loops to enable multiciliated cell gene expression. PLoS Genet 13, e1006538.

Rao VG, Subramanianbalachandar V, Magaj MM, Redemann S, Kulkarni SS (2023). Mechanisms of cilia regeneration in Xenopus multiciliated epithelium in vivo. bioRxiv, 544972.

Rosenbaum JL, Witman GB (2002). Intraflagellar transport. Nat Rev Mol Cell Biol 3, 813–825.

Sae-Lee W, McCafferty CL, Verbeke EJ, Havugimana PC, Papoulas O, McWhite CD, Houser JR, Vanuytsel K, Murphy GJ, Drew K, et al. (2022). The protein organization of a red blood cell. Cell Reports 40, 111103.

Schindelin J, Arganda-Carreras I, Frise E, Kaynig V, Longair M, Pietzsch T, Preibisch S, Rueden C, Saalfeld S, Schmid B, et al. (2012). Fiji: an open-source platform for biological-image analysis. Nat Methods 9, 676–682.

Seiler CY, Park JG, Sharma A, Hunter P, Surapaneni P, Sedillo C, Field J, Algar R, Price A, Steel J, et al. (2014). DNASU plasmid and

PSI:Biology-Materials repositories: resources to accelerate biological research. Nucleic Acids Res 42, D1253–D1260.

Seixas C, Casalou C, Melo LV, Nolasco S, Brogueira P, Soares H (2003). Subunits of the chaperonin CCT are associated with Tetrahymena microtubule structures and are involved in cilia biogenesis. Exp Cell Res 290, 303–321.

Signor D (1999). Role of a class DHC1b dynein in retrograde transport of IFT motors and IFT raft particles along cilia, but not dendrites, in chemosensory neurons of living Caenorhabditis elegans. J Cell Biol 147, 519–530.

Sim HJ, Yun S, Kim HE, Kwon KY, Kim G-H, Yun S, Kim BG, Myung K, Park TJ, Kwon T (2020). Simple method to characterize the ciliary proteome of multiciliated cells. J Proteome Res 19, 391–400.

Sung C-H, Leroux MR (2013). The roles of evolutionarily conserved functional modules in cilia-related trafficking. Nat Cell Biol 15, 1387–1397.

Taschner M (2017). Structural basis of outer dynein arm intraflagellar transport by the transport adaptor protein ODA16 and the intraflagellar transport protein IFT46. J Biol Chem 292, 7462–7473.

Taschner M, Lorentzen E (2016). The Intraflagellar transport machinery. Cold Spring Harb Perspect Biol 8, a028092.

The UniProt Consortium (2023). UniProt: the Universal Protein Knowledgebase in 2023. Nucleic Acids Res 51, D523–D531.

Tran PV, Haycraft CJ, Besschetnova TY, Turbe-Doan A, Stottmann RW, Herron BJ, Chesebro AL, Qiu H, Scherz PJ, Shah JV, et al. (2008). THM1 negatively modulates mouse sonic hedgehog signal transduction and affects retrograde intraflagellar transport in cilia. Nat Genet 40, 403–410.

Treutlein B, Brownfield DG, Wu AR, Neff NF, Mantalas GL, Espinoza FH, Desai TJ, Krasnow MA, Quake SR (2014). Reconstructing lineage hierarchies of the distal lung epithelium using single-cell RNA-seq. Nature 509, 371–375.

Tsao C-C, Gorovsky MA (2008). Tetrahymena IFT122A is not essential for cilia assembly but plays a role in returning IFT proteins from the ciliary tip to the cell body. J Cell Sci 121, 428–436.

Tu F, Sedzinski J, Ma Y, Marcotte EM, Wallingford JB (2018). Protein localization screening in vivo reveals novel regulators of multiciliated cell development and function. J Cell Sci 131, jcs206565.

Uhlén M, Fagerberg L, Hallström BM, Lindskog C, Oksvold P, Mardinoglu A, Sivertsson Å, Kampf C, Sjöstedt E, Asplund A, et al. (2015). Tissue-based map of the human proteome. Science 347, 1260419.

Vadnais ML, Cao W, Aghajanian HK, Haig-Ladewig L, Lin AM, Al-Alao O, Gerton GL (2014). Adenine nucleotide metabolism and a role for AMP in modulating flagellar waveforms in mouse sperm1. Biol Reprod 90, 128.

van Dam TJP, Kennedy J, Lee R van der, Vrieze E de, Wunderlich KA, Rix S, Dougherty GW, Lambacher NJ, Li C, Jensen VL, et al. (2019). CiliaCarta: An integrated and validated compendium of ciliary genes. PLoS One 14, e0216705.

Walentek P, Quigley IK (2017). What we can learn from a tadpole about ciliopathies and airway diseases: Using systems biology in Xenopus to study cilia and mucociliary epithelia. Genesis 55, e23001.

Walther Z, Vashishtha M, Hall JL (1994). The Chlamydomonas FLA10 gene encodes a novel kinesin-homologous protein. J Cell Biol 126, 175–188.

Wan C, Borgeson B, Phanse S, Tu F, Drew K, Clark G, Xiong X, Kagan O, Kwan J, Bezginov A, et al. (2015). Panorama of ancient metazoan macromolecular complexes. Nature 525, 339–344.

Wang W, Silva LM, Wang HH, Kavanaugh MA, Pottorf TS, Allard BA, Jacobs DT, Dong R, Cornelius JT, Chaturvedi A, et al. (2022). Ttc21b deficiency attenuates autosomal dominant polycystic kidney disease in a kidney tubular- and maturation-dependent manner. Kidney Int 102, 577–591.

Williams CL, McIntyre JC, Norris SR, Jenkins PM, Zhang L, Pei Q, Verhey K, Martens JR (2014). Direct evidence for BBSome-associated intraflagellar transport reveals distinct properties of native mammalian cilia. Nat Commun 5, 5813.

Wingfield JL, Lechtreck K-F, Lorentzen E (2018). Trafficking of ciliary membrane proteins by the intraflagellar transport/BBSome machinery. Essays Biochem 62, 753–763.

Yang Y, Park M, Maekawa M, Fairn GD (2019). Enforced expression of phosphatidylinositol 4-phosphate 5-kinase homolog alters PtdIns(4,5)P2 distribution and the localization of small G-proteins. Sci Rep 9, 14789.

Yeyati PL, et al. (2017). KDM3A coordinates actin dynamics with intraflagellar transport to regulate cilia stability. J Cell Biol 216, 999–1013.

Yu F, Li T, Sui Y, Chen Q, Yang S, Yang J, Hong R, Li D, Yan X, Zhao W, et al. (2020). O-GlcNAc transferase regulates centriole behavior and intraflagellar transport to promote ciliogenesis. Protein Cell 11, 852–857.

Yuan X, Zheng H, Su Y, Guo P, Zhang X, Zhao Q, Ge W, Li C, Xi Y, Yang X (2019). Drosophila Pif1A is essential for spermatogenesis and is the homolog of human CCDC157, a gene associated with idiopathic NOA. Cell Death Dis 10, 125.

Zhang X, Xiao Z, Zhang J, Xu C, Liu S, Cheng L, Zhou S, Zhao S, Zhang Y, Wu J, et al. (2022). Differential requirements of IQUB for the assembly of radial spoke 1 and the motility of mouse cilia and flagella. Cell Reports 41, 111683.